Role of Hydration in Magnesium versus Calcium Ion Pairing with Carboxylate: Solution and the Aqueous Interface

Maria G. Vazquez de Vasquez[a†], Bethany A. Wellen Rudd[b†], Marcel D. Baer[c], Emma E. Beasley[a], and Heather C. Allen[a*]

[a]Department of Chemistry & Biochemistry, The Ohio State University, Columbus, Ohio 43210, United States. [b]Department of Chemistry, Ohio Wesleyan University, Delaware, Ohio 43015, United States. [c] Physical Sciences Division, Pacific Northwest National Laboratory, Richland, Washington 99352,

[†]Authors contributed equally

[*]To whom correspondence may be addressed: allen@chemistry.ohio-state.edu

Abstract

The binding of group II metal cations such as Ca^{2+} and Mg^{2+} have been largely categorized as electrostatic or ionic using carboxylate symmetric and asymmetric stretching frequency assignments that have been historically used with little regard for the solvation environment on aqueous solutions. However, given the importance of these cations and their binding mechanisms related to biological function and in revealing surface enrichment factors for ocean to marine aerosol transfer, it is imperative that a deeper understanding be sought to include hydration effects. Here, infrared reflection-absorption and Raman spectra for surface and solution phase carboxylate binding information, respectively, are compared against bare (unbound) carboxylate and bi-dentate Zn^{2+} : carboxylate spectral signatures. Spectral non-coincidence effect analysis, temperature studies, and spectral and potential of mean force calculations result in a concise interpretation of binding motifs that include the role of mediating water molecules, that is, contact and solvent-shared ion pairs. Calcium directly binds to the carboxylate group in contact ion pairs where

magnesium rarely does. Moreover, we reveal the dominance of the solvent-shared ion pair of magnesium with carboxylate at the air-water interface and in solution.

Introduction

Ion-carboxylate coordination geometries/mechanisms in aqueous solutions were first methodically determined by comparing aqueous spectral responses to those of inorganic solid-state crystal structures of various metal carboxylates.[1–6] The traditional symmetric and asymmetric stretch frequency data markers are still commonly and pervasively being used as the primary metric for classifying the ion pairing of aqueous ion-carboxylates as ionic, mono-dentate, bi-dentate, or bridging with little regard to the vastly different hydration environments of these complexes in aqueous solutions compared to the solid state crystals from which the spectral markers are based.[7–16] Recently, critical analysis of this dated interpretation of spectral responses to ion-carboxylate interactions has been made through the use of gas phase cluster studies.[17] While this prior study gives insight to ion-carboxylate interactions and the spectroscopic intramolecular mechanism for the observed infrared frequencies, it has limitations in addressing hydration of the ion-carboxylate complex such that the aqueous phase is not fully captured. As infrared and Raman spectroscopy are not completely selective for informing or distinguishing between binding environments, including that of local hydration, a controversy still exists around the designation of the commonly called "ionic interaction" as either contact or solvent-shared ion pairing.

The binding of divalent cations, Ca^{2+} and Mg^{2+}, to negatively charged functional groups, such as carboxylate, has significant consequences in the structure and function of many systems of biological[18–24] and atmospheric interest.[25–33] In biology, Ca^{2+} and Mg^{2+} play important roles in ATP synthesis, cell proliferation, and receptor/target information pathways.[19,20,34–37] In addition to biological studies, the role of Ca^{2+} and Mg^{2+} in atmospheric aerosol chemistry is an important area of research. As bubbles burst at the ocean surface, aerosols are released to the atmosphere carrying with them enriched concentrations of surface-active organic molecules and inorganic ions. Despite its lesser concentration in bulk seawater (10 mM compared to 50 mM),[38,39] studies have shown that Ca^{2+} enrichment in sea spray aerosols is much higher than that of Mg^{2+}.[28,29] This likely indicates a preferential binding of Ca^{2+} ions to negatively charged surfactant headgroups at the air-sea interface,[40] thus leading to increased transfer of calcium ions to the aerosol phase. The binding of Ca^{2+} and Mg^{2+} to the carboxylate headgroups of marine prevalent fatty acids such as palmitic acid and stearic acid has significant effects on the organization and structure of organic films on sea spray aerosols thus impacting the climate properties of these particles.[26,28,29,33,41,42]

While this paper does not focus on calculating binding constants, prior solution and interfacial studies have been used to determine the binding constants of divalent metal cations to carboxylate groups.[29,43–49] Previously reported binding constants of Ca^{2+} and Mg^{2+} to short chain fatty acids in aqueous solutions have been shown to be identical.[50] Although, the binding constants provide a numerical value of the number of bound species, it does not necessarily equate to the number of bound species in a particular binding motif. To our knowledge, experimental spectra of both solution and interfacial regimes coupled with calculations have not been used together to elucidate the ion pairing details, including that of local hydration, of divalent metal cations interacting with carboxylate groups. In this work, both solution and interfacial spectroscopies are used to obtain a detailed molecular picture of the binding coordinations of Ca^{2+} and Mg^{2+} to carboxylate to inform on contact versus solvent mediated ion pairing. Previous literature has shown that Raman studies can provide carboxylate binding information about metal cations of different valencies,[51,52] although it is difficult to distinguish differences between metal cations of the same group without a priori information. Studies have shown that surface-sensitive techniques can extract additionally distinguishable spectral signatures of binding events between same-group cations and lipid headgroups. For example, same-group divalent cations have been shown to affect the stabilization of lipid monolayers by altering headgroup hydration despite their similar charge state and properties.[17,32,33,44,47,53–61] As the selection rules of IR and Raman spectroscopy results in the ability to observe different stretching vibrational modes (COO^- asymmetric in IR and the COO^- symmetric in Raman), these two techniques used in surface and solution environments, respectively, provide a more complete picture of the vibrational landscape of our systems of interest.

Here, we provide structural and energetic insights on the binding motifs of the carboxylate group with the biologically and atmospherically relevant group II metal cations, Ca^{2+} and Mg^{2+}. We compare the spectra of these cations with that of bare acetate and that of the strongly bound Zn^{2+} transition metal;[13,62] zinc's covalent binding structure is established. To evaluate solution and interfacial effects, we investigate acetate in the aqueous solution phase and long-chain carboxylic acid monolayers for interfacial studies. We use polarized Raman spectroscopy, coupled with deconvolution methods, to extract the free and ion-perturbed (contact and solvent-shared ion paired) carboxylate spectra. Free energy and spectral calculations describe binding motifs and are compared against the Raman solution and infrared interfacial experiments. Calculations are also used to elucidate the energy barrier for Mg^{2+} relative to Ca^{2+} for the number of first shell coordinated water molecules. Temperature studies track peak areas and frequencies to provide information on the hydration energetics of ion-bound populations. The interfacial infrared aqueous surface spectra, Raman solution spectra, and calculations reveal that Ca^{2+} and Mg^{2+} disclose unique $COO^-:M^{2+}$ spectral signatures, indicating both contact and solvent-shared binding environments for Ca^{2+}, yet, dominantly the solvent-shared binding environment for Mg^{2+}.

Experimental Methods

Infrared reflection-absorption spectroscopy measurements

Deuterated palmitic acid (C_{15}-COOH) (>98%, Cambridge Isotopes Laboratories) was dissolved in chloroform (HPLC Grade, Fisher Scientific) at a concentration of approximately 2 mM and was spread dropwise (Hamilton, 50 μL) to a mean molecular area of 20.5 Å^2/molecule onto the surface of a petri dish containing 0.3 M solutions of $MgCl_2 \cdot 6H_2O$ (>99%, ACS Certified, Fisher Scientific), $CaCl_2 \cdot 2H_2O$ (>99%, ACS Certified, Fisher Scientific), or $ZnCl_2$ (>98%, Acros Organics) prepared in D_2O (99%, Sigma Aldrich). Deuteration of both the lipid chain and the subphase was necessary to remove various modes (CH_2 scissoring mode at ~1460-1470 cm^{-1} and the positive H_2O bending mode at ~1650 cm^{-1}) from the spectral region of interest in the infrared reflection-absorption spectroscopy measurements. The use of D_2O also leads to an increased intensity of the observed bands in the spectra due to changes in subphase optical constants and reflectivities (**Fig. S1**).[8]

A custom-built setup consisting of two planar gold mirrors situated in an FTIR spectrometer (Spectrum 100, Perkin Elmer) was used to collect IRRAS spectra. The first gold mirror directs the incoming unpolarized IR beam to the sample surface at a 45° angle of incidence relative to surface normal. The second gold mirror then directs the reflected radiation to a liquid nitrogen cooled MCT detector. Adsorption of atmospheric water vapor to the D_2O surface can lead to HOD interferences in the spectra (**Fig. S2**). To minimize such interference, the spectrometer chamber was purged with a constant flow of nitrogen and sealed with plastic during the course of the measurement. Each spectrum was collected over the range of 4000-450 cm^{-1}, with 1 cm^{-1} step size, and resulted from coaveraging of 300 scans. The spectra presented here are the average of at least 3 individual trials which have been baseline corrected by a third-order polynomial prior to averaging. An example of a third-order polynomial fit (**Fig. S3**) used for baseline-subtraction of the IRRAS spectra is shown in the Supplemental Information. IRRAS spectra are represented in units of reflectance-absorbance ($RA = -\log(R/R_0)$), where the R is the reflectance of the monolayer-covered surface, and the reflectance of the bare surface is R_0.

Raman spectroscopy measurements

Sodium acetate ($NaCH_3COO$) (Sigma Aldrich) solution was dissolved in nanopure water with a resistivity of 18.2 MΩ·cm (Milli-Q Advantage A10, EMD Millipore, Billerica, MA, USA) at a concentration of 0.5 M. Metal carboxylate solutions were prepared by adding and appropriate mass of sodium acetate (Sigma Aldrich), and either magnesium chloride ($MgCl_2 \cdot 6H_2O$), calcium chloride ($CaCl_2 \cdot 2H_2O$), or zinc(II) chloride ($ZnCl_2$) (Sigma Aldrich) to a volumetric flask and completed with nanopure water to make a solution of 0.5M $NaCH_3COO$:0.25 M $MgCl_2$, $CaCl_2$, or $ZnCl_2$. All solutions were sonicated to for ~5 min to assist dissolution. Both the 0.5 M $NaCH_3COO$:0.25 M $MgCl_2$ and 0.5M $NaCH_3COO$:0.25 M $ZnCl_2$ solutions were passed through a 0.2 μm Whatman syringe filter (Sigma Aldrich). The filter was pre-wetted with each particular solution to avoid changes in concentration. All salts were used without further purification. The solutions were equilibrated to room temperature.

The polarized Raman spectra were collected using custom-build polarized Raman spectrometer consisting of a 532 nm diode pumped CW laser with a built-in laser line (±0.5) and polarization filters (>100:1 V, Crystalaser). Excitation was directly coupled with a custom-build fiber optic polarized Raman probe (InPhotonics) allowing 235 mW power to the sample at a range of 90-4200 cm^{-1}. Two outputs of scatter light a parallel polarized (V) and a perpendicular polarized (H) were sent to two independent FC fiber-optic end ports. The polarized output ports were fiber coupled to a spectrograph with a 600 lines mm^{-1} grating. The wavelength was calibrated to He:Ne emission lines (IsoPlane 320, Princeton Instruments) and detected using a liquid nitrogen cooled CCD detector (Pylon, 1340 x 400 pixel, Princeton Instruments). The coupling of the two 200 μm core fibers directly to the spectrograph allowed simultaneously collection of the perpendicular (HV) and parallel (VV) polarized spectra. Experiments were performed at the different temperatures, 21, 25, 30, 40, 50, 60, 70, 80 and 85 ºC. Spectra were collected by signal averaging 300 spectra each with a 0.5 s integration time. The Raman spectra presented here are the average of at least 3 individual trials which have been baseline corrected by fitting two end points to a line prior to averaging.

Theoretical Calculations

All Born-Oppenheimer *ab initio* molecular dynamics simulations were performed within the NVT (at 300 K) ensemble using periodic boundary conditions within the CP2K simulation suite (http:www.cp2k.org) containing the QuickStep module for the DFT calculations.[63] We used a double zeta basis set that has been optimized for the condensed phase[64] in conjunction with GTH pseudopotentials[65] with a 400 Ry cut-off for the auxiliary plane wave basis. The temperature was controlled with a Nose-Hoover thermostat[66] attached to every degree of freedom to ensure equilibration. The Becke[67] exchange and correlation due to Lee, Yang and Parr (LYP)[68] is utilized in addition to the dispersion correction (D2) put forth by Grimme[69] with a 40 ˚A cut-off.

The weighted histogram analysis method (WHAM)[70] was employed to extract a free energy profile from biased simulations for the coordination number (n) of water molecules around Mg^{2+} and the Mg-acetate binding.

Mg-coordination: Bulk simulations for the Mg^{2+} ion performed following similar protocol as in Baer et al. 2016.[71] The simulation cell consisted of single Mg^{2+} in 96 water molecules in a 14.4 $Å^3$box. The coordination number (n) is computed using the same functional form for as in a previous study.

$$\mathrm{n} = \sum_{i}^{N} \frac{1-(\frac{r_i}{r_0})^{16}}{(1-(\frac{r_i}{r_0})^{32}}$$

where N is the number of all water oxygen atoms, r_i is the distance between a given oxygen atom to the Mg^{2+}.The cutoff distance r_0 is set to 0.24 nm and the free energy is computed using the Umbrella sampling technique. Sampling windows for the n ranging from 4.9 to 7.1 were equally spaced by 0.1 apart employing harmonic Umbrella potentials of the from

$V(n) = k(n_0 - n)^2$ with a force constant k of 956 kcal mol^{-1}. In each Umbrella window a trajectory of at least 25 ps was collected after 5 ps of equilibration.

Mg-acetate binding: The acetate simulation cell consisted of one solute molecule in 95 water molecules and a single Mg^{2+} ion in a cubic box with the edge length of 14.40 Å. The free energy profiles for the C-cation interaction were obtained by Umbrella sampling. Sampling windows for the distance ranging from 2.4 to 5.6 Å were equally spaced by 0.2 Å employing harmonic Umbrella potentials of the from $V(r) = k(r_0 - r)^2$ with a force constant k of 9.56 kcal mol^{-1} $Å^{-2}$. To ensure sufficient sampling in the barrier region for the Ca^{2+} and Mg^{2+} additional windows with stiffer force constants were added ranging from 3.6 to 4.6 Å equally spaced 0.1 Å apart with a force constant of 33.46 kcal mol^{-1} $Å^{-2}$. In each Umbrella window a trajectory of at least 30 ps was collected after 5 ps of equilibration.

Ensembled averaged spectra for the acetate COO^- symmetric and asymmetric stretch were obtained following the same approach as for the Ca^{2+} in Denton et al. 2019[17] we harvested a series of configurations from the minima in the PMF simulations of aqueous acetate (with and without the presence of ions). The ensembles of configurations represent i) the isolated acetate anion, and ii) the Mg^{2+} ion in the bi-dentate (B), iii) mono-dentate (M), and iv) solvent-shared (SS) regimes. From the ensembles of configurations, the acetate only was optimized in the instantaneous environment aqueous environment and local harmonic frequencies computed.

Results and Discussion

The air-aqueous interface. At the interface, ion-carboxylate binding events can be studied with surface-sensitive spectroscopy techniques. To this end, infrared reflection-absorption spectroscopy (IRRAS) was used to investigate the binding of Ca^{2+} and Mg^{2+} ions to carboxylic acids at the air-aqueous interface. IRRAS spectra were collected of deuterated C_{16} carboxylic acid (C_{15}-COOH) monolayers spread on the surface of metal chloride ($CaCl_2$, $MgCl_2$, $ZnCl_2$) salt solutions in D_2O. The monolayers were spread to a target mean molecular area (20.5 $Å^2$/molecule) to guarantee full monolayer coverage of the aqueous interface. In this method of monolayer preparation there are no external perturbations (i.e., continuous compression) acting on the surfactant molecules to create an unstable, elevated surface pressure. These systems represent relaxed surface environments whose molecular organization can be more appropriately compared to their aqueous solution counterparts.

As has been reported extensively in the literature,[7,11,14,33,40,56,58,72,73] divalent ions induce the spontaneous deprotonation of long-chain carboxylic acid monolayers at the air-aqueous interface. The COO^- stretching region of the IRRAS spectra is shown in **Fig. 1**, demonstrating the ion-induced deprotonation of the C_{15}-COOH monolayers. The predominant feature in these spectra is the asymmetric stretch (ν_{AS}) of the COO^- group between 1500 cm^{-1} and 1625 cm^{-1}.[33,74] The intensity of the COO^- symmetric stretch (ν_S) is weak in infrared measurements, but can be seen at ~1425 cm^{-1}. Noise is greater around the ν_S mode due to its proximity to the region in which HOD interference is severe (1500-1200 cm^{-1}).[75]

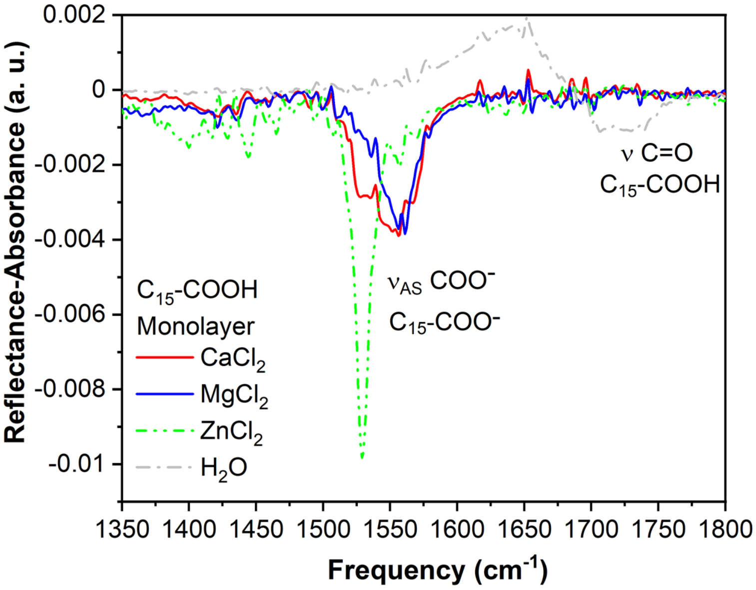

Figure 1. Infrared reflection spectra of deuterated C_{15}-COOH monolayers (20.5 Å^2/molecule) on 0.3 M solutions of $CaCl_2$ (red) and $MgCl_2$ (blue) in D_2O revealing ion-perturbed spectral responses of the ν_{AS} COO^- mode. The spectrum of the monolayer on a $ZnCl_2$ solution (green, dotted) is also shown for comparison and overlays the significant second band within the ν_{AS} mode in the $CaCl_2$ spectrum. The spectrum of a C_{15}-COOH monolayer on pure water (H_2O) is shown for comparison to demonstrate the lack of the COO^- mode when the monolayer is protonated. Additionally, the C=O stretch of the protonated carboxylic acid monolayer is not present in the ion-deprotonated spectra. The water bending mode at 1650 cm^{-1} is eliminated with the use of D_2O subphases.

Examination of the carboxylate ν_{AS} mode for Ca^{2+} and Mg^{2+} solutions in **Fig. 1** reveals unique ion-perturbed $COO^-:M^{2+}$ spectral signatures. The various degrees of broadening indicate the presence of multiple binding environments between the metal ions and carboxylate groups. The ν_{AS} mode of the C_{15}-COO^-:Mg^{2+} spectrum is centered at 1557 cm^{-1} and can be described as having asymmetry with greater intensity at higher frequencies. This spectrum is nearly identical to that of the bare carboxylate mode of a spread C_{18} monolayer (C_{17}-COOH, stearic acid) on a basic D_2O subphase previously reported in the literature,[17] thus highly suggestive of a largely hydrated, or solvent-mediated, binding environment.

The spectrum of C_{15}-COO^-:Ca^{2+} exhibits a broad ν_{AS} mode centered at 1551 cm^{-1}. This ν_{AS} mode extends to lower frequencies and exhibits a second band with significant intensity at approximately 1526 cm^{-1} that is not strongly present in the C_{15}-COO^-:Mg^{2+} spectrum. The binding of Zn^{2+} ions to carboxylate groups has been well studied and is characterized as a direct, chelating bi-dentate contact ion pair,[13,76] as such the spectrum of C_{15}-COO^-:Zn^{2+} is employed as a reference for spectral features associated with the more direct contact ion binding motif. Upon comparison of the C_{15}-COO^-:Ca^{2+} spectrum to the corresponding spectrum of C_{15}-COO^-:Zn^{2+}, it can be seen that the lower frequency region of the C_{15}-COO^-:Ca^{2+} complex directly overlays that of the C_{15}-COO^-:Zn^{2+} complex centered at 1529 cm^{-1}. The broadness of the ν_{AS} mode in the C_{15}-COO^-:Ca^{2+} spectrum to frequencies representative of the more direct binding motif similar to that of C_{15}-COO^-:Zn^{2+}, provides evidence to the presence of the differences in binding motifs that exist between the Ca^{2+} and Mg^{2+} ions and carboxylate groups at the air-aqueous interface. Based on the spectral responses in these systems, we claim, and later show additional evidence, that some fraction of C_{15}-COO^-:Ca^{2+} ion pairs exist as contact ion pairs in mono-dentate and/or bi-dentate geometries in addition to those complexed as solvent-shared ion pairs, whereas C_{15}-COO^-:Mg^{2+} ion pairs are primarily solvent-shared. To gain further insight to the coordination differences between Ca^{2+} and

Mg^{2+}, we turn to investigate these ion-perturbed carboxylate systems in bulk solution with Raman spectroscopy.

Solution studies of acetate. Polarized Raman spectroscopy was utilized to elucidate the binding motifs and local hydration of Ca^{2+} and Mg^{2+} to acetate in aqueous solutions of $CaCl_2$ and $MgCl_2$, respectively. For an individual aqueous metal acetate solution, the raw measured Raman spectrum includes features from both the ion-perturbed and free acetate, as well as the water molecules that are influenced by each of these species (**Figs. 2a** and **2b**). In all solutions, the intensities of the ν_S C-C (**Fig. 2a**) and ν_S COO^- mode **(Fig. 2b**) exhibit differences from that of acetate in pure water. Ben-Amotz and co-authors show that ν_S C-C and ν_S COO^- bands of sodium acetate do not change as a function of concentration and that Na^+ has an insignificant inference on water structure up to 2 M.[50] Thus, sodium acetate was chosen as the bare acetate spectrum due the lack of frequency shifts and its solvent-separated complexation of $COO^-:Na^+$.[77] Such lack of frequency shifts does not imply that Na^+ cannot bind to carboxylate since it has a binding affinity but simply it cannot be spectrally observed. Similarly to the IRRAS data, the corresponding Zn^{2+} spectrum is obtained as a comparison to the studies of Ca^{2+} and Mg^{2+}. There is no doubt that charge transfer occurs with Zn^{2+} as opposed to Ca^{2+} and Mg^{2+}. The Zn^{2+} spectrum shows the largest intensity change in both the ν_S C-C and ν_S COO^- modes implying that the Zn^{2+} ion interacts more strongly with acetate as is expected due to the 4s and 4p orbitals accepting the charge, thus leading to contact ion pairing.[13,45,46,50,78] The presence of Zn^{2+} in solution, (**Figs. 2a** and **2b**) clearly causes a blue shift in both modes (935.3 to 939.9 cm^{-1} and 1424.7 to 1427.6 cm^{-1}, respectively) and a suppression of the Raman transition moment strength representative of direct-contact ion pairing.

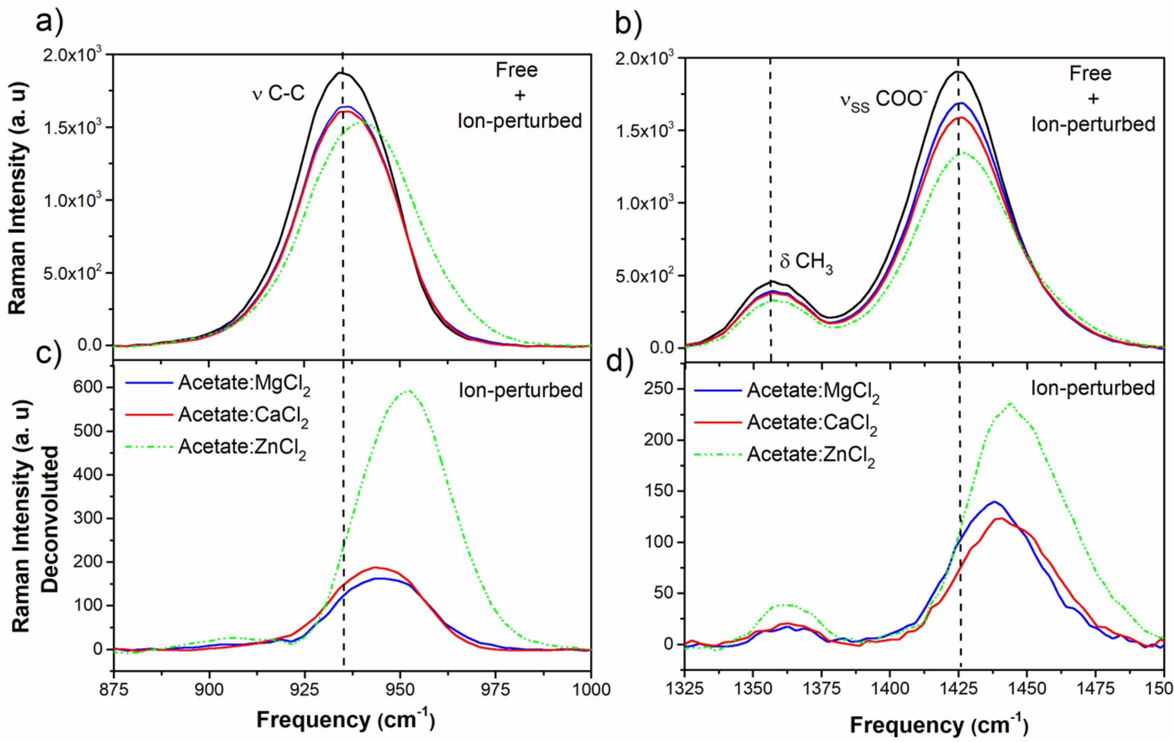

Figure 2. Polarized Raman spectra of the (a) ν_S C-C stretching mode and (b) ν_S COO$^-$ symmetric stretching mode of acetate in 0.25 M solutions of $MgCl_2$ (blue), $CaCl_2$ (red), $ZnCl_2$ (green dotted), and water (black, bare acetate) at 21°C. Dashed lines are drawn at the frequency of acetate in pure water for both ν_S C-C and ν_S COO$^-$. Upon the addition of salt, the intensity of these modes decreases in all solutions. The presence of Zn^{2+} ions in solution causes a significant blue shift of the modes, whereas the frequency of the modes is less affected by Ca^{2+} and Mg^{2+}. The deconvoluted polarized Raman spectra (c) and (d) show the ion-perturbed acetate systems associated with Zn^{2+}, Ca^{2+}, and Mg^{2+} in which frequency and intensity differences are more apparent for all ions.

It is evident that Ca^{2+} produces a slightly larger intensity change for the ν_S C-C and ν_S COO$^-$ than Mg^{2+} that can be attributed to the differences in binding environments. However, these changes are very small compared to those of Zn^{2+}, thus making ion-pairing assignments a challenge without further analysis of the spectra. Through deconvolution methods we removed the spectrum of the bare acetate from the COO$^-$:M^{2+}spectra (process described more thoroughly in the Supplemental Information) and extracted only the ion-perturbed carboxylate spectra associated with each divalent cation as shown **Figs. 2c** and **2d**. While the acetate:Zn^{2+} spectrum clearly shows the most dramatic change upon deconvolution due to the large fraction of covalently linked contact ion pairs in solution, the ion-perturbed carboxylate spectra of Ca^{2+} and Mg^{2+} complexes clearly show differences from each other, thus demonstrating variation in binding environments between

Mg^{2+} and Ca^{2+} ions with acetate in solution. We observe that the ν_S COO^- mode associated with Ca^{2+} tracks with the acetate:Zn^{2+} spectrum yet shifts to higher frequencies and is broader than that of acetate:Mg^{2+}, indicative of an additional population of contact ion pairs with Ca^{2+}. While the deconvoluted spectra point to differences between Ca^{2+} and Mg^{2+},solution Raman spectra alone may not necessarily be able to identify different ion pair structures. Multiple states contribute to the full spectrum, where some can be subtracted but the remainder constitutes an averaged ensemble in which ion pairs are weighed by their free energy. Thus, considering the interfacial spectra results as well as computational approaches can aid in identifying most probable ion pair structures.

To further elucidate hydration effects, polarized versus depolarized Raman spectra were evaluated in terms of the non-coincidence effect. Non-coincidence refers to the difference in frequency between the anisotropic and isotropic parts of the Raman scattering[79–83] and can provide insight into the binding motifs. The non-coincidence effect is a result of resonant transfer of vibrational excitation energy between the molecules coupled by hydrogen bonds, permanent dipole moments or any other interactions.[82] Prior studies have shown that hydrogen bond formation decreases the non-coincidence effect values where negative values can also be observed.[81,82,84] **Fig. S4** shows the spectra of the convoluted (free + ion-perturbed) and deconvoluted (ion-perturbed) in both polarizations. Here I_{VV} (incident light and scatter light are at 90 ° , both polarized vertically) and I_{VH} (incident light is polarized vertically and scattered light is polarized horizontal) were used rather than the I_{iso} ($I_{iso} = I_{VV} – (4/3)I_{HV}$) and I_{aniso} ($I_{aniso} = (4/3)I_{HV}$), which affects the intensity of the band and not its spectral position or frequency. Our spectra show a larger frequency shift in the I_{VH} than in the I_{VV} polarization that is observed in both the free + ion-perturbed and ion-perturbed spectra. The frequencies of each cation of the I_{VV} and the I_{VH} are plotted in **Fig. 3**

(spectra shown in Fig. **S4;** difference in **Fig. S5)** revealing that Mg^{2+} is the most resistant to changes in frequency, consistent with full hydration. The chemical environment and symmetry of the fully hydrated solvent-shared ion pair gives rise to relatively no deviation in frequency between the two polarization conditions, consistent with a steadfast hydrogen bonding environment around the Mg^{2+} ions. Zn^{2+} shows a frequency change because as the carboxylate binds to zinc the water-hydrogen-bonding network changes. Hydrogen bonding is disrupted as the ion sheds some of the solvating water molecules in order to bind with the carboxylate; therefore, an increase in the non-coincidence value is observed. Lastly, a plausible explanation for Ca^{2+} frequency differences are the largest because Ca^{2+} is more labile across two regimes: solvent-shared (fully hydrated) and contact ion paired.

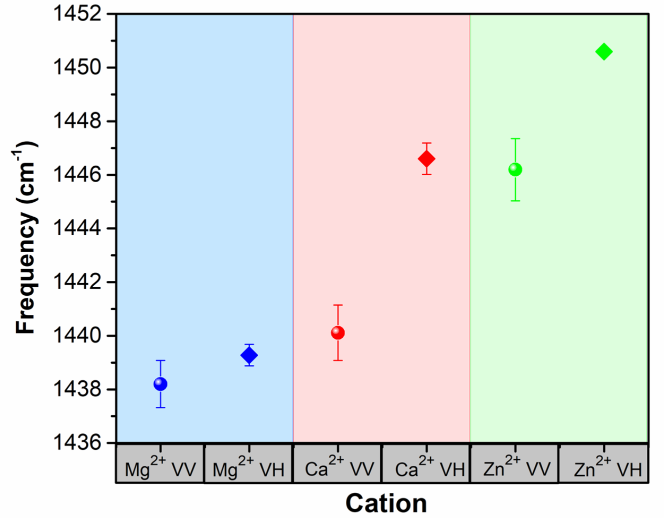

Figure 3. COO$^-$ ion-perturbed frequency of the I_{VV} and I_{VH} as a function of the cations in their respective VV/HV polarization. There is a negligible frequency change of ~1 cm^{-1} between I_{VV} and I_{VH} for Mg^{2+},whereas Ca^{2+} shows the largest change in frequency of ~6.5 cm^{-1}. Zn^{2+} is shown as a comparison as a bidentate motif showing a difference of ~ 4.4 cm^{-1}. Hydrogen bonding perturbations are captured in the frequency differences. Disruption of the H-bonding network is revealed through non-coincidence of the Raman polarized (VV) versus depolarized (VH) frequencies.

Taking the deconvoluted Raman spectra, we could not determine the fractions of solvent-shared, mono-dentate, and bi-dentate configurations; however, we can estimate the percentage of acetate molecules that are perturbed by an ion-carboxylate interaction in solvent-shared and, more generally, contact ion configurations . During the deconvolution process, a normalization factor representing the percentage of the free acetate in the COO^-:M^{2+} spectra was calculated between the bare acetate and the COO^-:M^{2+} spectra at the COO^- frequency (see SI for details). The remaining percent out of 100% represents the percent of acetate species in an ion-perturbed environment as shown in **Fig. 4a**, 12 % for Mg^{2+} and 17% for Ca^{2+}, presenting COO^-:Zn^{2+} as a reference for a more directly bound system as previously discussed.

For the surface measurements, as we are investigating an initially protonated long-chain carboxylic acid monolayer, the full ion-induced deprotonation observed in **Fig. 1** would correspond to 100% of carboxylate groups existing in an ion-perturbed environment. As the infrared measurements only show ion-induced deprotonation, 100% of the spectral response is associated with an ion-perturbed system (solvent-shared and contact ion paired) at the interface. We can conduct a similar analysis to the solution phase studies, yet instead specifically determine the percent of carboxylate groups in a contact ion paired binding motif. Briefly, the area of the ν_{AS} mode between 1500 and 1625 cm^{-1} in the spectrum of fully deprotonated stearic acid (C_{17}-COOH) on a basic D_2O subphase (**Fig. S6**) was used as a reference of the spectral response of a fully solvated carboxylate mode. This area was then subtracted from area of the ν_{AS} mode associated with the C_{15}-COOH monolayers on Mg^{2+} and Ca^{2+} solutions. Any remaining spectral area is attributed to a contact ion pair spectral response. This area is then normalized to the total area to yield an approximate percent of contact ion paired carboxylate species at the interface. For Mg^{2+}, an estimated 100% of ion-deprotonated carboxylate groups at the interface exist in a solvent-shared environment, whereas on Ca^{2+} solutions, approximately 18% of species exist in a contact ion pairing geometry (**Fig. 4b**). For comparison, the result for Zn^{2+} contact ion pairs is also shown for which a similar analysis was conducted between 1500 and 1580 cm^{-1}. While the Raman and IRRAS analysis produce two different insights into ion complexation (ion-perturbed vs. contact ion specifically), both the solution and surface measurements are in agreement that carboxylate groups are more so mediated by water with Mg^{2+} compared to Ca^{2+}, thus suggesting a greater fraction of species in a solvent-shared binding motif.

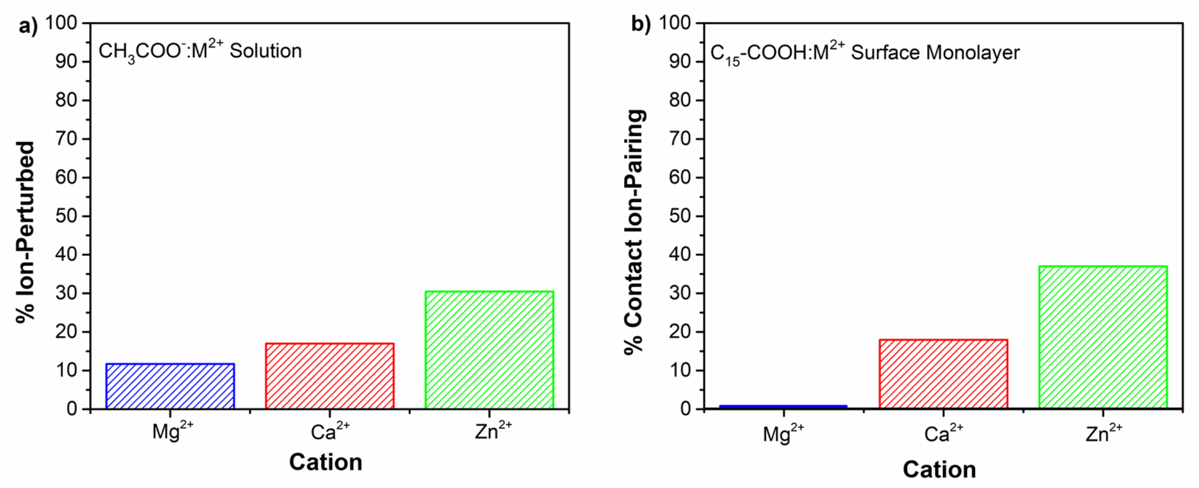

Figure 4. Comparison of a) the percentage of carboxylate species that are ion-perturbed either as solvent-shared or contact ion paired in solution, b) the percentage of carboxylate groups that are specifically contact ion paired at the interface.

Frequency Calculations. While the previously described Raman and surface IR experiments provide experimentally observed changes in the binding of divalent cations to carboxylic acids and carboxylate ions, an assignment of the complex structure is difficult. Particularly, spectra alone do not provide enough information to distinguish completely between the three different types of metal-carboxylate ion pairs: mono-dentate, bi-dentate, or solvent-shared ion pairs. Mono- and bi-dentate structures are contact ion pairs whereas solvent-shared ion pairs possess one water molecule that is coordinated to the cation and also hydrogen bonded to the carboxylate. To determine the spectral shift that is induced upon ion binding, ensemble frequencies based on quantum density functional theory (DFT) are computed. Here, spectral signatures are calculated for ensembles of structures corresponding to one of the three different ion pairs based on molecular dynamics simulations (MD). The simulations length using DFT MD does not allow for a sampling of transitions between the three ion pairs and estimate of their relative population. The relative population is calculated using Umbrella sampling, see below.

Frequencies for the acetate in the three binding motifs for Ca^{2+}, Mg^{2+}, Zn^{2+} are calculated for a large number of snapshots extracted from DFT MD (see Methods for details). The influences on the C-C stretch and the symmetric COO^- stretch as probed by Raman solution spectra have been discussed in detail in the literature following a similar approach.[50] It can be assumed that the observed C-C stretch band deviates from the unperturbed reference (940 cm^{-1}) the closer the cation is to the acetate. In line with this we see that the frequencies for the solvent-shared ion pairs (for all cations) are not significantly affected, yet are blue shifted for the contact ion pairs. This shift is more pronounced for Zn^{2+} and Mg^{2+} than Ca^{2+} and are larger for the bi-dentate than the mono-dentate ion pairs.

As discussed above, the surface IR spectra show a more pronounced effect for the asymmetric stretch of the deprotonated, ion-complexed carboxylic acid relative to the solution spectra. To elucidate the underpinnings of the spectral differences between Ca^{2+} and Mg^{2+} binding**,** a comparison of the computed and experimental frequencies is shown in **Fig. 5**. The observed shifts in the asymmetric stretch with Ca^{2+} have been discussed in detail in Denton at al. 2019.[17] All three binding motifs show distinct spectra, where the solvent-shared pair is blue shifted, the mono-dentate is not shifted with respect to the free acetate, and the bi-dentate is red shifted. Based on free-energy calculations, we assert that the Ca^{2+} is directly coordinated in mono- and bi-dentate contact ion pairs as well as solvent-shared pairs. This distribution readily fits the experimental spectra as shown in **Fig. 5**. Interestingly, for Mg^{2+} a red shift for the solvent-shared ion pair with respect to the free acetate and a blue shift for the mono-dentate is observed. Unlike for Ca^{2+} the mono-dentate structure is estimated to be dominant for Mg^{2+},[50] and the bi-dentate is not significantly populated for the used DFT functional. The resulting spectra for the bi-dentate is very broad spanning the range from 1500 to 1550 cm^{-1}. The calculated frequency of the mono-dentate structure matches the position of the experimental maximum for the Mg^{2+}. The Zn^{2+} bound spectra show a consistent red shift for all three moieties, increasing from the solvent-shared ion pair, to the mono-dentate and largest for the bi-dentate. Even though the calculated bi-dentate structure is very broad, the maximum aligns well with the experimental observed. We note that the intensity of ensemble frequencies corresponds to the probability of this frequency to be observed for a given structure. For a direct comparison with experimental intensities this frequency distribution needs to be weighted by the probability of the structure and the transition dipole moment for IR.

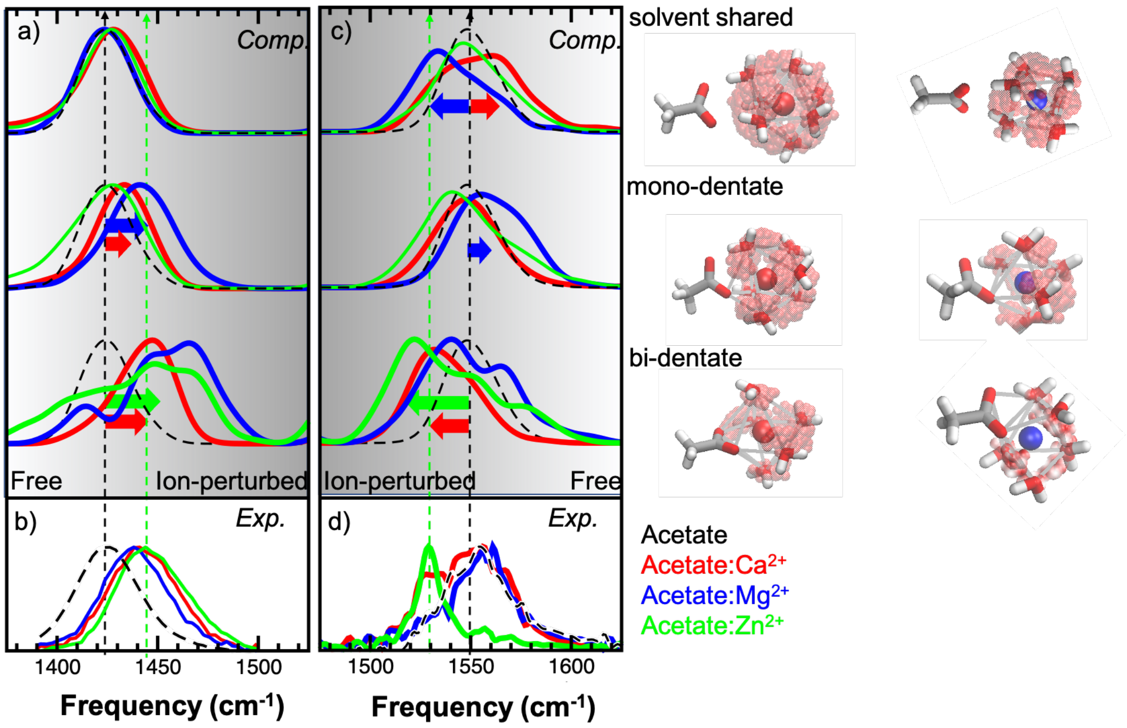

Figure 5. Comparison of calculated (a, c) acetate to experimental measured Raman spectra from Figure 2 for the symmetric COO$^-$ (b) stretch and infrared reflection spectra of deuterated C_{15}-COOH monolayers from Figure 1 for the asymmetric stretch (d). Ensemble averaged harmonic frequencies of the three binding motifs: solvent-shared ion pair, mono-dentate, bi-dentate and, and without ion bound (black) for three different ions Ca^{2+} (red), Mg^{2+} (blue), and Zn^{2+} (green) are shown in both panels compared the experimental spectra from top to bottom. Right panel shows the difference in local solvation structure for around Ca^{2+} (left) and Mg^{2+} (right) for the three binding motifs.

Free Energy Calculations The probability to find the contact ion pair versus the solvent-shared pair is calculated through the potential of mean force (PMF) along the distance between the metal ion and the acetate.[17,50,85] The resulting PMF is shown in **Fig. 6** show for both Ca^{2+} (**Fig. 6a**) and Mg^{2+} (**Fig. 6c**), showing for both a free-energetically stabilized bound state compared to the solvent-shared binding motif. Unlike the Ca^{2+}, which exhibits both mono- and bi-dentate binding motifs, the Mg^{2+} shows the mono-dentate binding only, in good agreement with earlier studies.[50] The change in solvation structure upon ion pair formation for Ca^{2+} was shown to be enabled by the rather flexible solvent shell around the cation.[71] The free energy of changing the number of water molecules in the first coordination sphere around the ion, as shown in **Fig. 6b**, as determined by DFT calculations reproduced EXAFS experimental estimates. Interestingly, the barrier in the binding PMF going from solvent-shared to bound state is on the same order as the water exchange under bulk solvation going from 7 to 6 water molecules. For Mg^{2+}, on the other hand, the predominant state is 6-fold coordinated under bulk solvation and water exchange is associated with a barrier of about 6 kcal/mol, almost 3 times higher than for Ca^{2+} . Similar energetic changes in the coordination number have been shown to control the potassium to sodium selectivity in potassium channels.[86] Closer analysis of the free energy calculation reveals that the transition state region around 3.8 nm (**Fig. 6c**) shows proper overlap in the reaction coordinate but shows a large dependence on the number of water molecules in the first shell around the Mg^{2+}. The coordination number of water molecules around the cation is an orthogonal variable that needs to be considered to fully describe the association process. Assuming a similar behavior as in the Ca^{2+} case, the calculated barrier for water exchange under solution conditions can be used to approximate the barrier for the transition from the solvent-shared minimum to the transition state to the ion paired motif. This indicates that the barrier for ion pairing in the PMF is underestimated, by up to 4 kcal/mol. This would change the population for the Mg^{2+} bound to carboxylate from an overestimated 80% in contact ion pairs to a more realistic 6% in closer agreement with our experimental findings.

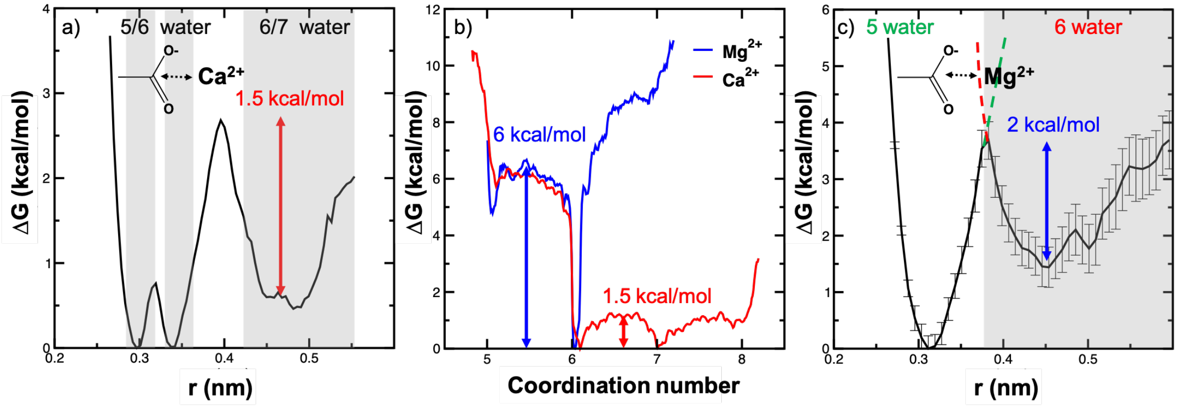

Figure 6. Potential of mean force for a) Ca^{2+} to acetate binding from Ref.,[17,85] b) changes in coordination number around Ca^{2+} (red, from Ref.[17,85]) and Mg^{2+} (blue) under bulk solvation, and c) Mg^{2+} to acetate binding. The shaded areas in a) and c) highlight distances with characteristic number of water molecules in the first solvation shell of the cation. Barriers associated with the transition from the solvent-shared to bound cation-acetate motif are highlighted with arrows, as well as corresponding free-energy barriers for associated with in water coordination number for the cations. For Mg^{2+} binding the dashed lines show extrapolated free-energy for fixed coordination number, indicating that barrier is underestimated.

The number of water molecules interacting with ions of size of the solvated complex (ion and first shell water molecules) are shown to correlate with the experimentally determined Jones-Dole B coefficient.[87] The B coefficient is interpreted as strength of the ion water interaction. In line with the larger barrier calculated for the water exchange for Mg^{2+} compared to Ca^{2+}, the experimental B coefficient for Mg^{2+} is larger than Ca^{2+}.[88] Even though both ions are of similar size an interesting temperature dependence is observed. The B coefficient is changing linear with increasing temperature for Ca^{2+}, but for Mg^{2+} a sudden change in slope is observed for temperatures over 30°C. This might indicate that the barrier for water exchange is temperature dependent.

Temperature-dependent acetate solution studies. In order to gain more information with respect to the energetics of binding motifs among divalent cations to carboxylate, Raman temperature-dependent measurements were implemented over a large temperature range (20-85 °C). The main goal for these temperature studies was to reveal the energy (temperature) needed for Mg^{2+} to shed one of it hydrating waters and form a direct contact ion pairing with aqueous carboxylate. Changes in frequency and peak area of the deconvoluted ion-perturbed carboxylate spectra were monitored. **Fig. 7** shows the changes in frequency of the ion-perturbed ν_S COO^- mode as a function of temperature. We can see that there is a red frequency shift for all solutions as temperature is increased, due to either the disorder induced by the increase in temperature and/or the weakening of ion-water bonds.[89,90] We can also clearly observe a frequency difference of ~14 cm^{-1} between bare acetate and ion-perturbed ν_S COO^- mode. The large frequency splitting between the ion-perturbed and the bare acetate spectra is due to the impact of bringing an ion close to the carboxylate. Desolvation also plays a role. As temperature is increased, the enhanced low frequency rattling motion of the ion in and out of proximity to the carboxylate results in a coupling and a frequency lowering of the ν_S COO^- mode. With bare acetate as the temperature is increased, minimal frequency lowering is observed as the coupling of the carboxylate mode to the water rattling motion is far less than that of a doubly charged ion.

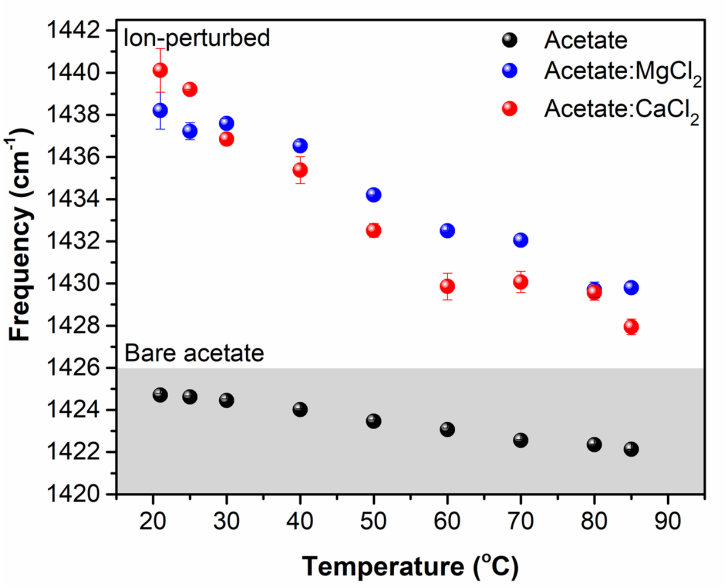

Figure 7. Raman spectral differences in frequency of the bare acetate COO$^-$ symmetric stretching mode (black) versus of the ion-perturbed acetate systems of 0.25 M solutions of $MgCl_2$ (blue), $CaCl_2$ (red) as a function of temperature. The ion-perturbed systems are referred to the deconvoluted spectra which is the result after subtraction of the bare acetate, see Supplemental Information for details on the deconvolution process. There is a large difference in frequency between the bare acetate and the ion-perturbed spectra due to the influence of bringing an ion close to the carboxylate.

Changes or differences in peak area of the ν_S COO$^-$ mode can shed light on the strength of the binding interactions between the divalent ions and carboxylate.[50] **Fig. 8** shows the peak area of ion-perturbed ν_S COO$^-$ mode of acetate in $CaCl_2$ (red) and $MgCl_2$ (blue) solutions. Our peak area analysis reveals that at 21 °C both acetate:Ca^{2+} and acetate:Mg^{2+} complexes have the same peak area suggesting a similar binding environment. However, as the temperature is increased, we see that the peak area of the acetate:Ca^{2+} complex increases more than that of acetate:Mg^{2+} suggesting possible differences in the amount of carboxylate being perturbed by the metal ion at that particular temperature. The increase in peak area of the ion-perturbed spectra with increasing temperature, which includes information on the FWHM, is correlated to an increase in the bound population. We also observe two slopes for the acetate:Mg^{2+} spectra. From 10 to 30 °C, no peak area increase is noted; however, after 30 °C a positive slope is observed, indicative of an increase in the number of binding events, and correlating with reported changes in the Jones-Dole B coefficient as described previously, whereas the acetate:Ca^{2+} spectra show only one positive slope indicating behavior that is not temperature sensitive. For both the Mg^{2+} and Ca^{2+} spectra, the slopes are similar for temperatures above 30 °C.

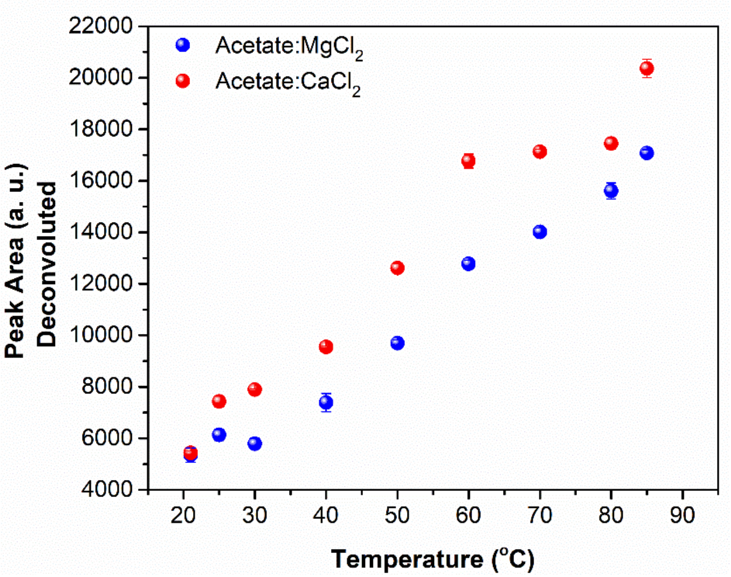

Figure 8. Peak area of the metal acetate after deconvolution of the ion-perturbed acetate as a function of temperature. This peak area increase of the ion perturbed spectra includes information of the FWHM which can be correlated to an increase in the bound population of the metal ion. Peak area data and the magnitude of the uncertainty (± 1 σ) are shown in Tables S1 and S2 for Ca^{2+} and Mg^{2+} cations.

Conclusions

Infrared reflection-absorption spectroscopy, polarized Raman, and theoretical calculations were used to determine the role of hydration in ion-carboxylate binding in both solution and interfacial aqueous environments. Our interfacial studies reveal differentiable spectral responses of the ion-carboxylate complexation. Two bands appear in the infrared reflection spectra strongly suggesting that a significant fraction of C_{15}-COO^-:Ca^{2+} bound complexes exist as contact ion pairs in mono-dentate and/or bi-dentate geometries in addition to those determined as solvent-shared ion pairs, whereas C_{15}-COO^-:Mg^{2+} complexes appear to primarily exist as solvent-shared ion pairs, i.e. C_{15}-

COO^- : H_2O : Mg^{2+}. To understand more generally the binding motifs, we further studied the simpler acetate solution using Raman spectroscopy. Free and ion-perturbed carboxylate spectra of acetate:M^{2+} solutions were extracted through spectral deconvolution methods. The ion-perturbed carboxylate spectra of acetate:Ca^{2+} and acetate:Mg^{2+} are significantly different, demonstrating variance in binding environment between both ions in acetate aqueous solution, albeit to a lesser extent to the trend observed at the interface. Moreover, analysis of the non-coincidence effect from polarized (and depolarized) Raman spectra revealed hydration differentiation of Mg versus Ca and Zn binding motifs, i.e. solvent-shared versus contact ion pairing, respectively. The invariability of the frequency of the magnesium – acetate system indicates a constant hydrogen bonding environment consistent with solvent sharing. However, large frequency differences between polarization conditions for both calcium and zinc ions demonstrate dehydration, thus indicate contact ion pairing. Importantly, we note that the interfacial environment is more efficient at binding both magnesium and calcium ions than in the solution phase environment. Calculations highlight the differences in the solvation structure of both ions and its effect on the binding of Ca^{2+} and Mg^{2+} to acetate. The large barrier for water exchange around Mg^{2+} has a large impact on the populations of ion binding motifs. Comparison of calculated spectra for Mg^{2+} and Ca^{2+} with both solution phase Raman and surface infrared reflection spectra leads to the picture in which Mg^{2+} is dominated by solvent-shared ion pairs.

Supplementary Materials

Data used to generate the experimental figures and conclusions in this manuscript are included in the Center for Aerosol Impacts on Chemistry of the Environment (CAICE) dataset at the UC San Diego Library Digital Collection website: https://doi.org/10.6075/J02807RK.

Authors Contributions

M. G. V. V. designed and conducted the Raman experiments with the assistance of E. E. B. M. G. V. V. preformed the data analysis for all Raman experiments. B. A. W. R. conducted the IRRAS experiments and analyzed the data. M. D. B. performed and analyzed theoretical calculation data. M. G. V. V., B. A. W. R., and M. D. B. wrote the manuscript with the input from all coauthors. H. C. A. conceived of the project, supervised the experiments, and edited the manuscript.

Conflicts of Interest

The authors declare no conflicts of interest.

Acknowledgements

Authors acknowledge funding for this work from the National Science Foundation Center for Aerosol Impacts on Chemistry of the Environment (NSF-CAICE) under Award No. CHE-1801971. M.D.B. was supported by the US Department of Energy, Office of Basic Energy Sciences, Biomolecular Materials Program at Pacific Northwest National Laboratory (PNNL); PNNL is operated by Battelle Memorial Institute for the US Department of Energy under Contract DE-AC05-76RL01830. The free energy calculations used resources of the National Energy Research Scientific Computing Center (NERSC), a U.S. Department of Energy Office of Science User Facility operated under Contract No. DE-AC02-05CH11231. The authors thank K. Carter-Fenk, L. Yan, M. Rogers, T. Adel, B. Vasquez, and Christopher Mundy for insightful comments.

References:

(1) Tackett, J. E. FT-IR Characterization of Metal Acetates in Aqueous Solution. *Appl Spectrosc* **1989**, *43* (3), 483–489. https://doi.org/10.1366/0003702894202931.

(2) Nakamoto, K.; Fujita, J.; Tanaka, S.; Kobayashi, M. Infrared Spectra of Metallic Complexes. IV. Comparison of the Infrared Spectra of Unidentate and Bidentate Metallic Complexes. *J. Am. Chem. Soc.* **1957**, *79* (18), 4904–4908. https://doi.org/10.1021/ja01575a020.

(3) Fujita, J.; Nakamoto, K.; Kobayashi, M. Infrared Spectra of Metallic Complexes. III. The Infrared Spectra of Metallic Oxalates. *J. Phys. Chem.* **1957**, *61* (7), 1014–1015. https://doi.org/10.1021/j150553a045.

(4) Nakamoto, K.; Morimoto, Y.; Martell, A. E. Infrared Spectra of Aqueous Solutions. I. Metal Chelate Compounds of Amino Acids. *J. Am. Chem. Soc.* **1961**, *83* (22), 4528–4532. https://doi.org/10.1021/ja01483a009.

(5) Kishida, S.; Nakamoto, K. Normal Coordinate Analyses of Hydrogen-Bonded Compounds. II. Dimeric Formic Acid and Acetic Acid. *J. Chem. Phys.* **1964**, *41* (6), 1558–1563. https://doi.org/10.1063/1.1726122.

(6) Nakamoto, K.; Kishida, S. Normal Coordinate Analyses of Hydrogen-Bonded Compounds. I. Monomeric Formic Acid and Acetic Acid. *J. Chem. Phys.* **1964**, *41* (6), 1554–1558. https://doi.org/10.1063/1.1726121.

(7) Brauner, J. W.; Flach, C. R.; Xu, Z.; Bi, X.; Lewis, R. N. A. H.; McElhaney, R. N.; Gericke, A.; Mendelsohn, R. Quantitative Functional Group Orientation in Langmuir Films by Infrared Reflection−Absorption Spectroscopy: CO Groups in Behenic Acid Methyl Ester and Sn2-13C-DSPC. *J. Phys. Chem. B* **2003**, *107* (29), 7202–7211. https://doi.org/10.1021/jp030066r.

(8) Flach, C. R.; Gericke, A.; Mendelsohn, R. Quantitative Determination of Molecular Chain Tilt Angles in Monolayer Films at the Air/Water Interface: Infrared Reflection/Absorption Spectroscopy of Behenic Acid Methyl Ester. *J. Phys. Chem. B* **1997**, *101* (1), 58–65. https://doi.org/10.1021/jp962288d.

(9) Gericke, A.; Flach, C. R.; Mendelsohn, R. Structure and Orientation of Lung Surfactant SP-C and L-Alpha-Dipalmitoylphosphatidylcholine in Aqueous Monolayers. *Biophys. J.* **1997**, *73* (1), 492–499. https://doi.org/10.1016/S0006-3495(97)78087-1.

(10) Gericke, A.; Mendelsohn, R. Partial Chain Deuteration as an IRRAS Probe of Conformational Order of Different Regions in Hexadecanoic Acid Monolayers at the Air/Water Interface. *Langmuir* **1996**, *12* (3), 758–762. https://doi.org/10.1021/la950608z.

(11) Gericke, A.; Michailov, A. V.; Hühnerfuss, H. Polarized External Infrared Reflection-Absorption Spectrometry at the Air/Water Interface: Comparison of Experimental and Theoretical Results for Different Angles of Incidence. *Vib. Spectrosc.* **1993**, *4* (3), 335–348. https://doi.org/10.1016/0924-2031(93)80007-3.

(12) Gericke, A.; Moore, D. J.; Erukulla, R. K.; Bittman, R.; Mendelsohn, R. Partially Deuterated Phospholipids as IR Structure Probes of Conformational Order in Bulk and Monolayer Phases. *Journal of Molecular Structure* **1996**, *379* (1), 227–239. https://doi.org/10.1016/0022-2860(95)09201-3.

(13) Simon-Kutscher, J.; Gericke, A.; Hühnerfuss, H. Effect of Bivalent Ba, Cu, Ni, and Zn Cations on the Structure of Octadecanoic Acid Monolayers at the Air−Water Interface As

Determined by External Infrared Reflection−Absorption Spectroscopy. *Langmuir* **1996**, *12* (4), 1027–1034. https://doi.org/10.1021/la950731q.

(14) Gericke, A.; Huehnerfuss, H. In Situ Investigation of Saturated Long-Chain Fatty Acids at the Air/Water Interface by External Infrared Reflection-Absorption Spectrometry. *J. Phys. Chem.* **1993**, *97* (49), 12899–12908. https://doi.org/10.1021/j100151a044.

(15) Robertson, E. J.; Beaman, D. K.; Richmond, G. L. Designated Drivers: The Differing Roles of Divalent Metal Ions in Surfactant Adsorption at the Oil–Water Interface. *Langmuir* **2013**, *29* (50), 15511–15520. https://doi.org/10.1021/la403665n.

(16) Nara, M.; Torii, H.; Tasumi, M. Correlation between the Vibrational Frequencies of the Carboxylate Group and the Types of Its Coordination to a Metal Ion: An Ab Initio Molecular Orbital Study. *J. Phys. Chem.* **1996**, *100* (51), 19812–19817. https://doi.org/10.1021/jp9615924.

(17) Denton, J. K.; Kelleher, P. J.; Johnson, M. A.; Baer, M. D.; Kathmann, S. M.; Mundy, C. J.; Wellen Rudd, B. A.; Allen, H. C.; Choi, T. H.; Jordan, K. D. Molecular-Level Origin of the Carboxylate Head Group Response to Divalent Metal Ion Complexation at the Air–Water Interface. *PNAS* **2019**, *116* (30), 14874–14880. https://doi.org/10.1073/pnas.1818600116.

(18) Clapham, D. E. Calcium Signaling. *Cell* **2007**, *131* (6), 1047–1058. https://doi.org/10.1016/j.cell.2007.11.028.

(19) Brini, M.; Calì, T.; Ottolini, D.; Carafoli, E. Intracellular Calcium Homeostasis and Signaling. In *Metallomics and the Cell*; Banci, L., Ed.; Metal Ions in Life Sciences; Springer Netherlands: Dordrecht, 2013; pp 119–168. https://doi.org/10.1007/978-94-007-5561-1_5.

(20) de Baaij, J. H. F.; Hoenderop, J. G. J.; Bindels, R. J. M. Magnesium in Man: Implications for Health and Disease. *Physiol. Rev.* **2015**, *95* (1), 1–46. https://doi.org/10.1152/physrev.00012.2014.

(21) Gifford, J. L.; Walsh, M. P.; Vogel, H. J. Structures and Metal-Ion-Binding Properties of the Ca2+-Binding Helix–Loop–Helix EF-Hand Motifs. *Biochem. J.* **2007**, *405* (2), 199–221. https://doi.org/10.1042/BJ20070255.

(22) Hsiao, C.; Williams, L. D. A Recurrent Magnesium-Binding Motif Provides a Framework for the Ribosomal Peptidyl Transferase Center. *Nucleic Acids Res.* **2009**, *37* (10), 3134–3142. https://doi.org/10.1093/nar/gkp119.

(23) Gresh, N.; Garmer, D. R. Comparative Binding Energetics of Mg^{2+}, Ca^{2+}, Zn^{2+}, and Cd^{2+} to Biologically Relevant Ligands: Combined Ab Initio SCF Supermolecule and Molecular Mechanics Investigation. *J. Comput. Chem.* **1996**, *17* (12), 1481–1495. https://doi.org/10.1002/(SICI)1096-987X(199609)17:12<1481::AID-JCC7>3.0.CO;2-G.

(24) Project, E.; Nachliel, E.; Gutman, M. The Dynamics of Ca2+ Ions within the Solvation Shell of Calbindin D9k. *PLoS One* **2011**, *6* (2). https://doi.org/10.1371/journal.pone.0014718.

(25) Cravigan, L. T.; Mallet, M. D.; Vaattovaara, P.; Harvey, M. J.; Law, C. S.; Modini, R. L.; Russell, L. M.; Stelcer, E.; Cohen, D. D.; Olsen, G.; Safi, K.; Burrell, T. J.; Ristovski, Z. Sea Spray Aerosol Organic Enrichment, Water Uptake and Surface Tension Effects. *Atmospheric Chem. Phys.* **2020**, *20* (13), 7955–7977. https://doi.org/10.5194/acp-20-7955-2020.

(26) Glass, S. J.; Matteson, M. J. Ion Enrichment in Aerosols Dispersed from Bursting Bubbles in Aqueous Salt Solutions. *Tellus* **1973**, *25* (3), 272–280. https://doi.org/10.1111/j.2153-3490.1973.tb00611.x.

(27) Guasco, T. L.; Cuadra-Rodriguez, L. A.; Pedler, B. E.; Ault, A. P.; Collins, D. B.; Zhao, D.; Kim, M. J.; Ruppel, M. J.; Wilson, S. C.; Pomeroy, R. S.; Grassian, V. H.; Azam, F.; Bertram, T. H.; Prather, K. A. Transition Metal Associations with Primary Biological Particles in Sea Spray Aerosol Generated in a Wave Channel. *Environ. Sci. Technol.* **2014**, *48* (2), 1324–1333. https://doi.org/10.1021/es403203d.

(28) Jayarathne, T.; Sultana, C. M.; Lee, C.; Malfatti, F.; Cox, J. L.; Pendergraft, M. A.; Moore, K. A.; Azam, F.; Tivanski, A. V.; Cappa, C. D.; Bertram, T. H.; Grassian, V. H.; Prather, K. A.; Stone, E. A. Enrichment of Saccharides and Divalent Cations in Sea Spray Aerosol During Two Phytoplankton Blooms. *Environ. Sci. Technol.* **2016**, *50*, 11511–11520. https://doi.org/10.1021/acs.est.6b02988.

(29) Salter, M. E.; Hamacher-Barth, E.; Leck, C.; Werner, J.; Johnson, C. M.; Riipinen, I.; Nilsson, E. D.; Zieger, P. Calcium Enrichment in Sea Spray Aerosol Particles: Calcium Enrichment in Sea Spray Aerosol. *Geophys. Res. Lett.* **2016**, *43*, 8277–8285. https://doi.org/10.1002/2016GL070275.

(30) Schill, S. R.; Burrows, S. M.; Hasenecz, E. S.; Stone, E. A.; Bertram, T. H. The Impact of Divalent Cations on the Enrichment of Soluble Saccharides in Primary Sea Spray Aerosol. *Atmosphere* **2018**, *9* (12), 476. https://doi.org/10.3390/atmos9120476.

(31) Xu, G.; Gao, Y. Atmospheric Trace Elements in Aerosols Observed over the Southern Ocean and Coastal East Antarctica. *Polar Res.* **2014**, *33* (1), 23973. https://doi.org/10.3402/polar.v33.23973.

(32) Zhang, T.; Fiamingo, M.; Allen, H. C. Trace Metal Enrichment Driven by Phosphate Functional Group Binding Selectivity. *J. Geophys. Res. Oceans* **2018**, *123* (8), 5286–5297. https://doi.org/10.1029/2018JC013926.

(33) Wellen Rudd, B. A.; Vidalis, A. S.; Allen, H. C. Thermodynamic versus Non-Equilibrium Stability of Palmitic Acid Monolayers in Calcium-Enriched Sea Spray Aerosol Proxy Systems. *Phys. Chem. Chem. Phys.* **2018**, *20* (24), 16320–16332. https://doi.org/10.1039/C8CP01188E.

(34) Jahnen-Dechent, W.; Ketteler, M. Magnesium Basics. *Clin. Kidney J.* **2012**, *5* (Suppl 1), i3–i14. https://doi.org/10.1093/ndtplus/sfr163.

(35) Yamanaka, R.; Shindo, Y.; Oka, K. Magnesium Is a Key Player in Neuronal Maturation and Neuropathology. *Int. J. Mol. Sci.* **2019**, *20* (14). https://doi.org/10.3390/ijms20143439.

(36) Neuhaus, G.; Bowler, C.; Kern, R.; Chua, N.-H. Calcium/Calmodulin-Dependent and -Independent Phytochrome Signal Transduction Pathways. *Cell* **1993**, *73* (5), 937–952. https://doi.org/10.1016/0092-8674(93)90272-R.

(37) Eldik, L. V.; Eldik, L. J. V.; Watterson, D. M. *Calmodulin and Signal Transduction*; Gulf Professional Publishing, 1998.

(38) Bruland, K. W. Trace Elements in Sea-Water. In *Chemical Oceanography*; Riley, J. P., Chester, R., Eds.; Academic Press, London, 1983; Vol. Vol. 8, pp 157–220. https://doi.org/10.1016/B978-0-12-588608-6.50009-2.

(39) Bruland, K. W.; Lohan, M. C. 6.02 - Controls of Trace Metals in Seawater. In *Treatise on Geochemistry*; Holland, H. D., Turekian, K. K., Eds.; Pergamon: Oxford, 2003; pp 23–47. https://doi.org/10.1016/B0-08-043751-6/06105-3.

(40) Adams, E. M.; Allen, H. C. Palmitic Acid on Salt Subphases and in Mixed Monolayers of Cerebrosides: Application to Atmospheric Aerosol Chemistry. *Atmosphere* **2013**, *4* (4), 315–336. https://doi.org/10.3390/atmos4040315.

(41) Cochran, R. E.; Laskina, O.; Jayarathne, T.; Laskin, A.; Laskin, J.; Lin, P.; Sultana, C.; Lee, C.; Moore, K. A.; Cappa, C. D.; Bertram, T. H.; Prather, K. A.; Grassian, V. H.; Stone, E. A. Analysis of Organic Anionic Surfactants in Fine and Coarse Fractions of Freshly Emitted Sea Spray Aerosol. *Environ. Sci. Technol.* **2016**, *50* (5), 2477–2486. https://doi.org/10.1021/acs.est.5b04053.

(42) Cochran, R. E.; Laskina, O.; Trueblood, J. V.; Estillore, A. D.; Morris, H. S.; Jayarathne, T.; Sultana, C. M.; Lee, C.; Lin, P.; Laskin, J.; Laskin, A.; Dowling, J. A.; Qin, Z.; Cappa, C. D.; Bertram, T. H.; Tivanski, A. V.; Stone, E. A.; Prather, K. A.; Grassian, V. H. Molecular Diversity of Sea Spray Aerosol Particles: Impact of Ocean Biology on Particle Composition and Hygroscopicity. *Chem* **2017**, *2* (5), 655–667. https://doi.org/10.1016/j.chempr.2017.03.007.

(43) Martinek, T.; Duboué-Dijon, E.; Timr, Š.; Mason, P. E.; Baxová, K.; Fischer, H. E.; Schmidt, B.; Pluhařová, E.; Jungwirth, P. Calcium Ions in Aqueous Solutions: Accurate Force Field Description Aided by Ab Initio Molecular Dynamics and Neutron Scattering. *J. Chem. Phys.* **2018**, *148* (22), 222813. https://doi.org/10.1063/1.5006779.

(44) Duboué-Dijon, E.; Mason, P. E.; Fischer, H. E.; Jungwirth, P. Hydration and Ion Pairing in Aqueous Mg2+ and Zn2+ Solutions: Force-Field Description Aided by Neutron Scattering Experiments and Ab Initio Molecular Dynamics Simulations. *J. Phys. Chem. B* **2018**, *122* (13), 3296–3306. https://doi.org/10.1021/acs.jpcb.7b09612.

(45) Smith, R. M.; Martell, A. E. Inorganic Ligands. In *Critical Stability Constants: Inorganic Complexes*; Smith, R. M., Martell, A. E., Eds.; Springer US: Boston, MA, 1976; pp 1–129. https://doi.org/10.1007/978-1-4757-5506-0_1.

(46) Bunting, J. W.; Thong, K. M. Stability Constants for Some 1:1 Metal–Carboxylate Complexes. *Can. J. Chem.* **1970**, *48* (11), 1654–1656. https://doi.org/10.1139/v70-273.

(47) Stumpff, F.; McGuigan, J. A. S. Measuring Ca^{2+} Binding to Short Chain Fatty Acids and Gluconate with a Ca^{2+} Electrode: Role of the Reference Electrode. *Anal. Biochem.* **2014**, *459*, 46–52. https://doi.org/10.1016/j.ab.2014.05.001.

(48) Edwards, D. A.; Hayward, R. N. Transition Metal Acetates. *Can. J. Chem.* **1968**, *46* (22), 3443–3446. https://doi.org/10.1139/v68-572.

(49) Dudev, T.; Lim, C. Principles Governing Mg, Ca, and Zn Binding and Selectivity in Proteins. *Chem. Rev.* **2003**, *103* (3), 773–788. https://doi.org/10.1021/cr020467n.

(50) Oliveira, D. M. de; Zukowski, S. R.; Palivec, V.; Hénin, J.; Martinez-Seara, H.; Ben-Amotz, D.; Jungwirth, P.; Duboué-Dijon, E. Binding of Divalent Cations to Acetate: Molecular Simulations Guided by Raman Spectroscopy. *Phys. Chem. Chem. Phys.* **2020**, *22* (41), 24014–24027. https://doi.org/10.1039/D0CP02987D.

(51) Otero, V.; Sanches, D.; Montagner, C.; Vilarigues, M.; Carlyle, L.; Lopes, J. A.; Melo, M. J. Characterisation of Metal Carboxylates by Raman and Infrared Spectroscopy in Works of Art. *J. Raman Spectrosc.* **2014**, *45* (11–12), 1197–1206. https://doi.org/10.1002/jrs.4520.

(52) Deacon, G. B.; Phillips, R. J. Relationships between the Carbon-Oxygen Stretching Frequencies of Carboxylato Complexes and the Type of Carboxylate Coordination. *Coord. Chem. Rev.* **1980**, *33* (3), 227–250. https://doi.org/10.1016/S0010-8545(00)80455-5.

(53) Adrian-Scotto, M.; Mallet, G.; Vasilescu, D. Hydration of Mg++: A Quantum DFT and Ab Initio HF Study. *J. Mol. Struct. THEOCHEM* **2005**, *728* (1), 231–242. https://doi.org/10.1016/j.theochem.2005.02.006.

(54) DePalma, J. W.; Kelleher, P. J.; Tavares, L. C.; Johnson, M. A. Coordination-Dependent Spectroscopic Signatures of Divalent Metal Ion Binding to Carboxylate Head Groups: H_2 - and He-Tagged Vibrational Spectra of $M^{2+} \cdot RCO_2^{-}$ (M = Mg and Ca, R = $-CD_3$, $-CD_2CD_3$) Complexes. *J. Phys. Chem. Lett.* **2017**, *8* (2), 484–488. https://doi.org/10.1021/acs.jpclett.6b02964.

(55) II, D. W. D.; Pedersen, L. G. The First Solvation Shell of Magnesium and Calcium Ions in a Model Nucleic Acid Environment: An Ab Initio Study. *J. Biomol. Struct. Dyn.* **1995**, *13* (1), 167–180. https://doi.org/10.1080/07391102.1995.10508828.

(56) Adams, E. M.; Casper, C. B.; Allen, H. C. Effect of Cation Enrichment on Dipalmitoylphosphatidylcholine (DPPC) Monolayers at the Air-Water Interface. *J. Colloid Interface Sci.* **2016**, *478*, 353–364. https://doi.org/10.1016/j.jcis.2016.06.016.

(57) Adams, E. M.; Verreault, D.; Jayarathne, T.; Cochran, R. E.; Stone, E. A.; Allen, H. C. Surface Organization of a DPPC Monolayer on Concentrated $SrCl_2$ and $ZnCl_2$ Solutions. *Phys. Chem. Chem. Phys.* **2016**, *18* (47), 32345–32357. https://doi.org/10.1039/C6CP06887A.

(58) Adams, E. M.; Wellen, B. A.; Thiraux, R.; Reddy, S. K.; Vidalis, A. S.; Paesani, F.; Allen, H. C. Sodium–Carboxylate Contact Ion Pair Formation Induces Stabilization of Palmitic Acid Monolayers at High PH. *Phys. Chem. Chem. Phys.* **2017**, *19*, 10481–10490. https://doi.org/10.1039/C7CP00167C.

(59) Casper, C. B.; Verreault, D.; Adams, E. M.; Hua, W.; Allen, H. C. Surface Potential of DPPC Monolayers on Concentrated Aqueous Salt Solutions. *J. Phys. Chem. B* **2016**, *120*, 2043–2052. https://doi.org/10.1021/acs.jpcb.5b10483.

(60) Zhang, T.; Cathcart, M. G.; Vidalis, A. S.; Allen, H. C. Cation Effects on Phosphatidic Acid Monolayers at Various PH Conditions. *Chem. and Phys. Lipids* **2016**, *200*, 24–31. https://doi.org/10.1016/j.chemphyslip.2016.06.001.

(61) Zhang, X.; Kumar, R.; Kuroda, D. G. Acetate Ion and Its Interesting Solvation Shell Structure and Dynamics. *J. Chem. Phys.* **2018**, *148* (9), 094506. https://doi.org/10.1063/1.5019363.

(62) Grigor'ev, A. I. Infrared Absorption Spectra of Acetated of Elements in Groups I and II of the Periodic System. *Russ. J. Inorg. Chem.* **1963**, *8* (4), 409–414.

(63) VandeVondele, J.; Krack, M.; Mohamed, F.; Parrinello, M.; Chassaing, T.; Hutter, J. Quickstep: Fast and Accurate Density Functional Calculations Using a Mixed Gaussian and Plane Waves Approach. *Comput. Phys. Commun* **2005**, *167* (2), 103–128. https://doi.org/10.1016/j.cpc.2004.12.014.

(64) VandeVondele, J.; Hutter, J. Gaussian Basis Sets for Accurate Calculations on Molecular Systems in Gas and Condensed Phases. *J. Chem. Phys.* **2007**, *127* (11), 114105. https://doi.org/10.1063/1.2770708.

(65) Goedecker, S.; Teter, M.; Hutter, J. Separable Dual-Space Gaussian Pseudopotentials. *Phys. Rev. B* **1996**, *54* (3), 1703–1710. https://doi.org/10.1103/PhysRevB.54.1703.

(66) Martyna, G. J.; Klein, M. L.; Tuckerman, M. Nosé–Hoover Chains: The Canonical Ensemble via Continuous Dynamics. *J. Chem. Phys.* **1992**, *97* (4), 2635–2643. https://doi.org/10.1063/1.463940.

(67) Becke, A. D. Density-Functional Exchange-Energy Approximation with Correct Asymptotic Behavior. *Phys. Rev. A* **1988**, *38* (6), 3098–3100. https://doi.org/10.1103/PhysRevA.38.3098.

(68) Lee, C.; Yang, W.; Parr, R. G. Development of the Colle-Salvetti Correlation-Energy Formula into a Functional of the Electron Density. *Phys. Rev. B* **1988**, *37* (2), 785–789. https://doi.org/10.1103/PhysRevB.37.785.

(69) Grimme, S. Accurate description of van der Waals complexes by density functional theory including empirical corrections. *J. Comput. Chem* **2004**, *25* (12), 1463–1473. https://doi.org/10.1002/jcc.20078.

(70) Grossfield, A. WHAM: An Implementation of the Weighted Histogram Analysis Method, Version 2.0.2, 2011.

(71) Baer, M. D.; Mundy, C. J. Local Aqueous Solvation Structure Around Ca^{2+} During $Ca^{2+}\cdots Cl^-$ Pair Formation. *J. Phys. Chem. B* **2016**, *120* (8), 1885–1893. https://doi.org/10.1021/acs.jpcb.5b09579.

(72) Carter-Fenk, K. A.; Allen, H. C. Collapse Mechanisms of Nascent and Aged Sea Spray Aerosol Proxy Films. *Atmosphere* **2018**, *9*, 503. https://doi.org/10.3390/atmos9120503.

(73) Perkins, R. J.; Vazquez de Vasquez, M. G.; Beasley, E. E.; Hill, T. C. J.; Stone, E. A.; Allen, H. C.; DeMott, P. J. Relating Structure and Ice Nucleation of Mixed Surfactant Systems Relevant to Sea Spray Aerosol. *J. Phys. Chem. A* **2020**, *124* (42), 8806–8821. https://doi.org/10.1021/acs.jpca.0c05849.

(74) Tang, C. Y.; Huang, Z.; Allen, H. C. Binding of Mg^{2+} and Ca^{2+} to Palmitic Acid and Deprotonation of the COOH Headgroup Studied by Vibrational Sum Frequency Generation Spectroscopy. *J. Phys. Chem. B* **2010**, *114* (51), 17068–17076. https://doi.org/10.1021/jp105472e.

(75) Desmeules, P.; Penney, S.-É.; Desbat, B.; Salesse, C. Determination of the Contribution of the Myristoyl Group and Hydrophobic Amino Acids of Recoverin on Its Dynamics of Binding to Lipid Monolayers. *Biophys. J.* **2007**, *93* (6), 2069–2082. https://doi.org/10.1529/biophysj.106.103481.

(76) Poyton, M. F.; Pullanchery, S.; Sun, S.; Yang, T.; Cremer, P. S. Zn^{2+} Binds to Phosphatidylserine and Induces Membrane Blebbing. *J. Am. Chem. Soc.* **2020**, *142* (43), 18679–18686. https://doi.org/10.1021/jacs.0c09103.

(77) Tang, C. Y.; Allen, H. C. Ionic Binding of Na^+ versus K^+ to the Carboxylic Acid Headgroup of Palmitic Acid Monolayers Studied by Vibrational Sum Frequency Generation Spectroscopy. *J. Phys. Chem. A* **2009**, *113* (26), 7383–7393. https://doi.org/10.1021/jp9000434.

(78) He, H.-T.; Xing, L.-C.; Zhang, J.-S.; Tang, M. Binding Characteristics of Cd^{2+}, Zn^{2+}, Cu^{2+}, and Li^+ with Humic Substances: Implication to Trace Element Enrichment in Low-Rank Coals. *Energy Explor. Exploit.* **2016**, *34* (5), 735–745. https://doi.org/10.1177/0144598716656067.

(79) Fini, G.; Mirone, P.; Fortunato, B. Evidence for Short-Range Orientation Effects in Dipolar Aprotic Liquids from Vibrational Spectroscopy. Part 1. - Ethylene and Propylene Carbonates. *J. Chem. Soc. Faraday Trans. 2* **1973**, *69*, 1243–1248. https://doi.org/10.1039/F29736901243.

(80) Mirone, P.; Fini, G. Local Order and Vibrational Coupling in Solutions of Polar Molecules. *J. Chem. Phys.* **1979**, *71* (5), 2241–2243. https://doi.org/10.1063/1.438557.

(81) Bhattacharjee, D.; Ghosh (Purkayastha), A.; Misra, T. N.; Nandy, S. K. The Non-Coincidence Effect in Polar Liquids. *Spectrochim. Acta A Mol. Biomol. Spectrosc.* **1995**, *51* (14), 2539–2543. https://doi.org/10.1016/0584-8539(95)01518-3.

(82) Kecki, Z.; Sokołowska, A. Crossing of Anisotropic and Isotropic Raman Components in the Intermolecular Resonance Coupling of Vibrations. IV—Methanol Solutions in Acetone. *J. Raman Spectrosc* **1996**, *27* (5), 429–432. https://doi.org/10.1002/(SICI)1097-4555(199605)27:5<429::AID-JRS981>3.0.CO;2-O.

(83) Sokołowska, A. Raman Study of the Influence of KCl and KI on Polarization Contours of OH Stretching Band of Water. *J. Raman Spectrosc.* **1996**, *27* (8), 621–624. https://doi.org/10.1002/(SICI)1097-4555(199608)27:8<621::AID-JRS4>3.0.CO;2-J.

(84) Thomas, H. D.; Jonas, J. Hydrogen Bonding and the Raman Noncoincidence Effect. *J. Chem. Phys.* **1989**, *90* (8), 4632–4633. https://doi.org/10.1063/1.456605.

(85) Daily, M. D.; Baer, M. D.; Mundy, C. J. Divalent Ion Parameterization Strongly Affects Conformation and Interactions of an Anionic Biomimetic Polymer. *J. Phys. Chem. B* **2016**, *120* (9), 2198–2208. https://doi.org/10.1021/acs.jpcb.5b12277.

(86) Varma, S.; Rempe, S. B. Tuning Ion Coordination Architectures to Enable Selective Partitioning. *Biophysical Journal* **2007**, *93* (4), 1093–1099. https://doi.org/10.1529/biophysj.107.107482.

(87) Baer, M. D.; Mundy, C. J. An Ab Initio Approach to Understanding the Specific Ion Effect. *Faraday Discuss.* **2013**, *160* (0), 89–101. https://doi.org/10.1039/C2FD20113E.

(88) Jenkins, H. D. B.; Marcus, Y. Viscosity B-Coefficients of Ions in Solution. *Chem. Rev.* **1995**, *95* (8), 2695–2724. https://doi.org/10.1021/cr00040a004.

(89) Bulmer, J. T.; Irish, D. E.; Ödberg, L. The Temperature Dependence of Raman Band Parameters for Aquated Mg(II) and Zn(II). *Can. J. Chem.* **1975**, *53* (24), 3806–3811. https://doi.org/10.1139/v75-550.

(90) Deng, G.-H.; Shen, Y.; Chen, H.; Chen, Y.; Jiang, B.; Wu, G.; Yang, X.; Yuan, K.; Zheng, J. Ordered-to-Disordered Transformation of Enhanced Water Structure on Hydrophobic Surfaces in Concentrated Alcohol–Water Solutions. *J. Phys. Chem. Lett.* **2019**, *10* (24), 7922–7928. https://doi.org/10.1021/acs.jpclett.9b03429.

TOC Graphic